Correlation analysis of the wind of a cable-stayed bridge based on field monitoring

Hui Li*[1], Shujin Laima[1], Na Li[2], Jinping Ou[1,3] and Zhondong Duan[1]

[1]School of Civil Engineering, Harbin Institute of Technology, Harbin, 150090, China
[2]CCCC Highway Consultants CO., LTD, Beijing, 100088, China
[3]School of Civil and Hydraulic Engineering, Dalian University of Technology, Dalian, 116024, China

Abstract. This paper investigates the correlation of wind characteristics monitored on a cable-stayed bridge. Total five anemoscopes are implemented into the bridge. Two out of 5 anemoscopes in inflow and two out of 5 anemoscopes in wake-flow along the longitudinal direction of the bridge are installed. Four anemoscopes are respectively distributed at two cross-sections. Another anemoscope is installed at the top of the tower. The correlation of mean wind speed and direction, power spectral density, the turbulent intensity and integral length of wind in flow at two cross-sections are investigated. In addition, considering the non-stationary characteristics of wind, the spatial correlation in time-frequency is analyzed using wavelet transform and different phenomenon from those obtained through FFT is observed. The time-frequency analysis further indicates that intermittence, coherence structures and self-similar structures are distinctly observed from fluctuant wind. The flow characteristics around the bridge deck at two positions are also investigated using the field measurement. The results indicate that the mean wind speed decrease when the flow passing through the deck, but the turbulence intensity become much larger and the turbulence integral lengths become much smaller compared with those of inflow. The relationship of RMS (root mean square) of wake-flow and the mean wind speed of inflow is approximately linear. The special structures of wake-flow in time-frequency domain are also analyzed using wavelet transform, which aids to reveal the forming process of wake-flow.

Keywords: field measurement; spatial correlation; time-frequency characteristics; flow characteristics.

1. Introduction

Recently, a number of long-span bridges have been constructed or are planning to be constructed in China, such as the Sutong Bridge with the longest central span in cable-stayed bridges, the Xihoumen Bridge with a central span of 1650 m and ranking No. 2 in suspension bridges, the Hangzhou Bay Bridge with the longest length in cross-strait bridges and the Hong Kong-Macao-Zhuhai Cross-strait Bridge (under planning). With increase in span of bridges, the bridges become more flexible and have small damping. Therefore, the bridges are more readily oscillate dramatically subjected to wind, i.e., the wind becomes the dominant load for the design of bridges. The wind tunnel test technology and CFD (computational fluid dynamics) are two powerful tools to

---

* Corresponding Author, Professor, E-mail: lihui@hit.edu.cn

investigate wind and wind effects on bridges. However, due to the limitation of wind tunnel test technology (such as size effect), and the computational cost, accuracy and reliability of CFD, the field monitoring for wind and wind effects of bridges is very important for understating the wind characteristics, wind effects and their mechanism of bridges. It is also a tool to validate the wind tunnel testing results and simulation results.

Full-scale measurements for wind effects on several long-span bridges have been conducted in previous research. Bietry *et al.* (1995) investigated the wind field characteristics and wind effects on the Saint-Nazaire Bridge. Turbulence intensity, turbulence integral scale and spatial correlation of the fluctuant wind were obtained through analyzing the recorded wind. The lateral and vertical nature frequencies and corresponding damping ratio were also analyzed based on the measured bridge oscillation and compared with those obtained with quasi-steady aerodynamic approach. The comparison indicated that the measured vertical and lateral frequencies and vertical damping ratio are consistent with the calculated results. However, the measured lateral damping ratio is much higher than the calculation results. The results also presented that the equal-steady theory neglecting the influence of aerodynamic admittance is conservative. Frandsen (2001) measured the wind pressures at the deck surface and accelerations simultaneously on the Great Belt East Suspension Bridge (the central span is 1624 m). The phenomenon of cross-wind vortex-induced oscillation was observed in smooth flow, low wind speed (around 8 m/s) with the corresponding direction perpendicular to the bridge line. It is confirmed from the results of full-scale measurements that the correlation of pressures and accelerations are very low outside lock-in region, however, in lock-in region, the correlation between them become strong. As the increase of turbulence intensity, the correlation between them decreases. Miyata *et al.* (2002) investigated the full-scale spatial correlation of the fluctuant wind along the Akashi-Kaikyo Bridge (the main span is 1991 m) during strong typhoons. The results indicated that the coherence of the longitudinal fluctuant wind at two positions does not go to unity with the frequency approaching to zero and there is no distinct trend of the decay factors (extensively used in the exponential formula) with respect to the distance, while the mean value of the decay factors at a distance slightly increases as the distance increases. In addition, the decay factors show a slightly increasing trend with the increase of mean wind speed. Xu and Zhu (2005) analyzed the wind velocities and bridge responses measured by the Wind and Structural Health Monitoring System of the Ting Ma Bridge during Typhoon Sam. A fitting target function was established through analyzing the PSD of the fluctuant wind and the spectra can fit the measured spectral data well in both low- and high-frequency regions. In addition, the Von Karman spectral is fitted with the auto-spectra better than the Kaimal and Simiu spectra, especially in the low frequency region, and the Kaimal spectra is fitted well with the measured co-spectrum and quadrature spectrum between every two of the three fluctuant wind components. Ni *et al.* (2007) investigated the wind-induced modal variability of a cable-stay bridge based on one-year monitoring data. It is revealed there is not explicit relationship between the modal frequencies and wind intensity.

Although some progresses in full-scale monitoring for wind and wind effects of long-span bridges have been made, the field monitoring of wind and wind effects of long-span bridges is still very insufficient. Fortunately, most long-span bridges have been implemented with structural health monitoring systems (including monitoring system of wind and wind effects), especially in china, which provide opportunities to investigate the wind characteristics and wind effects in real bridges (Ko and Ni 2005, Li *et al.* 2006, Azarbayejani *et al.* 2009, Jang *et al.* 2010, Ou and Li 2010). One cable-stayed bridge with single tower is selected as the case study in this paper. The cable-stayed bridge locates in Shenzhen and is a linking of Shenzhen and the Hong Kong. As one part of series

of monitoring results, the correlation of wind at different positions both inflow and wake-flow is the concerned issue in this study. In addition, the non-stationary of wind is also investigated based on the recorded wind.

2. Field measurements

The investigated bridge, as shown in Fig. 1, crossing over the Shenzhen Bay, linking between Shekou and Hong Kong, (Fig. 2), is an important corridor for the Hong Kong and Shenzhen. The total length of the bridge is 5.545 km. The bridge has two navigation channels, located in Shenzhen and the Hong Kong, respectively. One located in Shenzhen is the concerned bridge of this study. This bridge has three spans with the lengths of 180+90+75 m, as shown in Fig. 3. The tower is reinforced concrete structure with a height of 158.0 m. The inverted trapezoidal steel box girder with projecting slab is 38.6 m wide and 4.12 m high, as presented in Fig. 4.

To monitor the structural health status of the bridge, a structural health monitoring system was installed on the bridge by China Highway Planning and Design Institute. In the system, there were 5 anemometers and 30 uniaxial accelerometers. 4 Yong Model 8100 ultrasonic anemometers
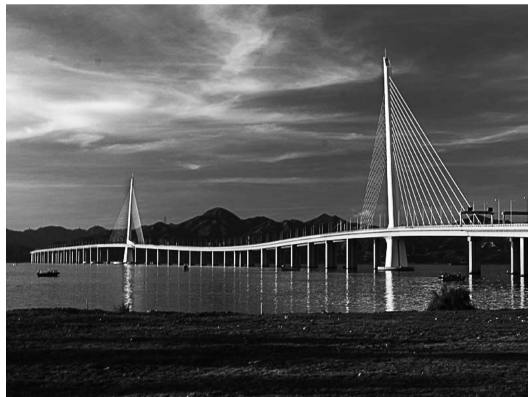

Fig. 1 The investigated bridge

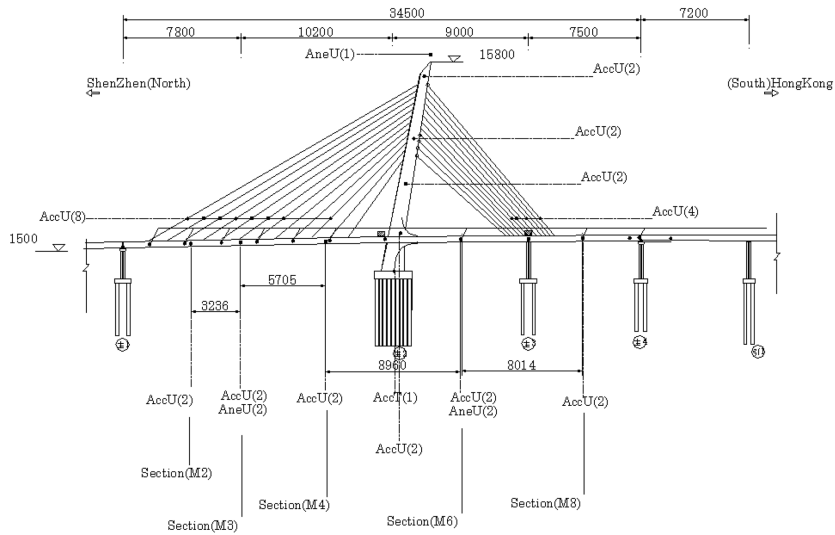Fig. 2 The location of the investigated bridge

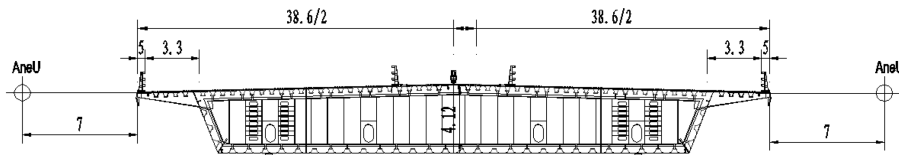Fig. 3 Bridge elevation and sensor arrangement

Fig. 4 Cross section of the deck

(a)Young Model 8100
ultrasonic anemometer

(b)Young Model 05103
propeller anemometer

Fig. 5 Anemometers used in the monitoring system

(AneU), as shown in Fig. 5(a), were installed at section M3 and section M6, respectively. At each section, one anemometer was located in east side, and the other was located in west side, each anemometer is 7 m far from the deck (as shown in Figs. 3 and 4). The measurement range of the ultrasonic anemometers is [0~40 m/s]. Each ultrasonic anemometer can measure three components of wind velocity, i.e., u_x, u_y and u_z. u_x, u_y and u_z respectively denote the crossing-bridge, along-

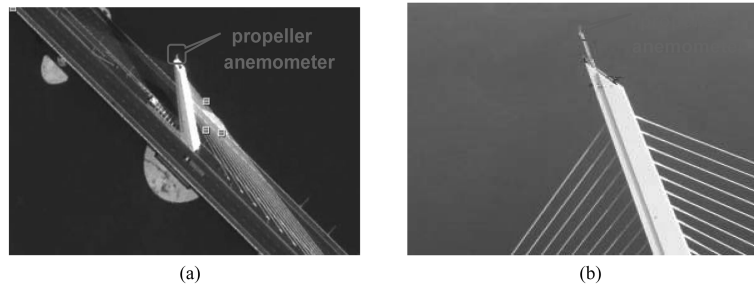(a)   (b)

Fig. 6 The location of propeller anemometer on the tower

bridge and vertical wind velocity. 1 Yong Model 05103 propeller anemometer (AneM) as shown in Fig. 5(b) was installed at the top of the tower (5 m departing from the tower), the location as shown in Fig. 6. AneM can measure the horizontal wind velocity and wind direction. The measurement range is [0~60 m/s]. The sampling frequencies were set as 10 and 1.67 Hz for the ultrasonic and propeller anemometers, respectively.

In the study, recorded data from this monitoring system for 3 successive days are analyzed. The record time ranged from 0:26:26, 17 August 2007 to 0:26:26, 20 August 2007.

3. Correlation of inflow along the bridge length

3.1 Mean wind speed and wind direction

The horizontal mean wind speed U and mean wind direction Φ in an elementary time interval can be determined by the following equations

$$U = \sqrt{(\bar{u}_x)^2 + (\bar{u}_y)^2} \tag{1}$$

$$\Phi = \begin{cases} ar\cos\dfrac{\bar{u}_x}{U} & if(u_y > 0) \\[2mm] 360 - ar\cos\dfrac{\bar{u}_x}{U} & if(u_y < 0) \end{cases} \tag{2}$$

where $\bar{u}_x$ and $\bar{u}_y$ are the mean values of recorded wind speed u_x and u_y in a time interval, such as 10 min here.

The fluctuating wind velocity $u(t)$, $v(t)$, $w(t)$ can be calculated by

$$\begin{aligned} u(t) &= u_x \cos\Phi + u_y \sin\Phi - U \\ v(t) &= -u_x \sin\Phi + u_y \cos\Phi \\ w(t) &= u_z - \bar{u}_z \end{aligned} \tag{3}$$

Where $u(t)$, $v(t)$, $w(t)$ represent longitudinal, lateral and vertical fluctuation wind velocity in an elementary interval, respectively.
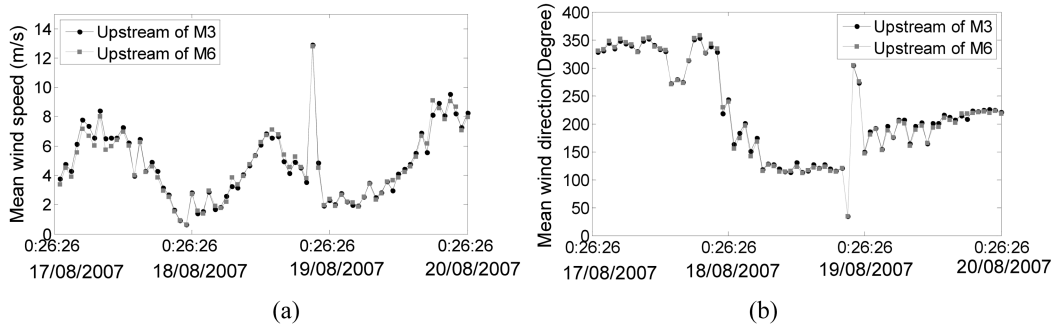
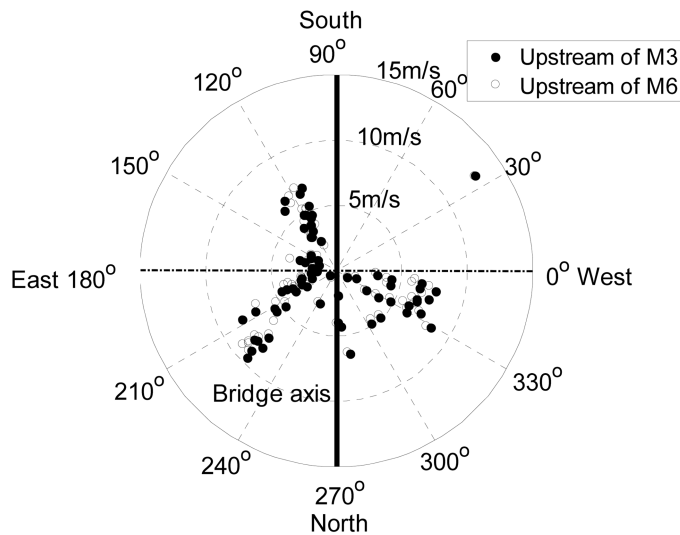Fig. 7 (a) Variations of 10- min mean wind speed and (b) mean wind direction with time

Fig. 8 Wind rose diagram during the measured period

Fig. 7 shows the variations of 10-min mean wind speed and mean wind direction with time at upstream of sections M3 and M6, respectively. At upstream of M3, the maximum 10-min mean wind speed is 12.87 m/s and the average is 4.70 m/s; while at upstream of M6, the maximum 10-min mean wind speed is 12.82 m/s and the average is 4.64 m/s. In the three days, the wind directions are unstable. On 17 August 2007, the mean wind direction is 321° at M3 upstream, and 323° at M6 upstream, On 18 August 2007, the mean wind direction is 143° at M3 upstream, and 141° at M6 upstream, On 19 August 2007, the mean wind direction is 202° at M3 upstream, and 199° at M6 upstream. Fig. 8 gives wind rose diagram during the measured period. It is found that the mean wind speeds and directions measured from the two anemometers are very similar. Therefore, the wind can be regarded as having the same characteristics in mean wind speed and wind direction along the bridge length.

3.2 Mean wind profile

The mean wind profile is assumed to follow the power law and may be fitted by the following formula

$$\frac{U_Z}{U_{Z_0}} = \left(\frac{Z}{Z_0}\right)^{\alpha} \tag{4}$$

where U_z is the mean wind speed at the height of Z; U_{Z_0} is the mean wind speed at reference height of Z_0.

Fig. 9 shows the variations of 10-min mean wind speed at upstream of M6, M3 and the top of the tower. According to the mean wind speeds of these two positions, the power exponent may be obtained by Eq. (4). Fig. 10 presents the mean wind profile for M6-T0 and M3-T0 (T0 means the tower), the solid line denotes $\alpha = 0.12$, which is adopted in the Load Design Code for Structures (GB5009-2001, 2002, China) for the sea surface. The ratio of U_z to U_{Z_0} during the record time is also given in Fig. 10. The average power exponent is 0.1214 at upstream of M3, close to 0.12. While, at upstream of M6, the average power exponent is 0.1314, which is slightly larger than 0.12, it may be attributed to the anemometer at M6 is closer to the tower than the one at M3 and the tower has more impact on the wind at upstream of M6. Fig. 11 denotes the relationship between mean wind speed and power exponent when the mean wind speed above 4 m/s. The result indicates
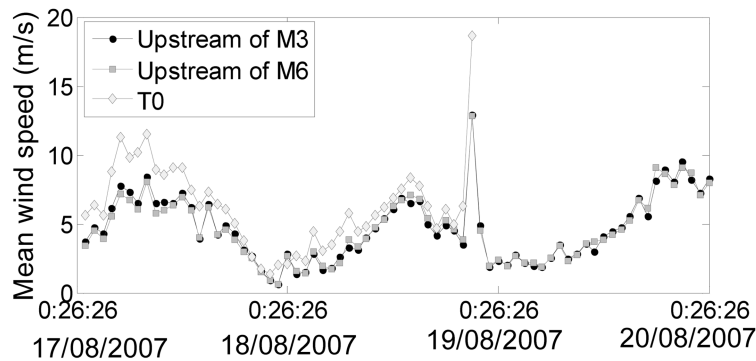

Fig. 9 Variation of 10-min mean wind speeds measured at upstream of M6, M3 and the top of tower, T0
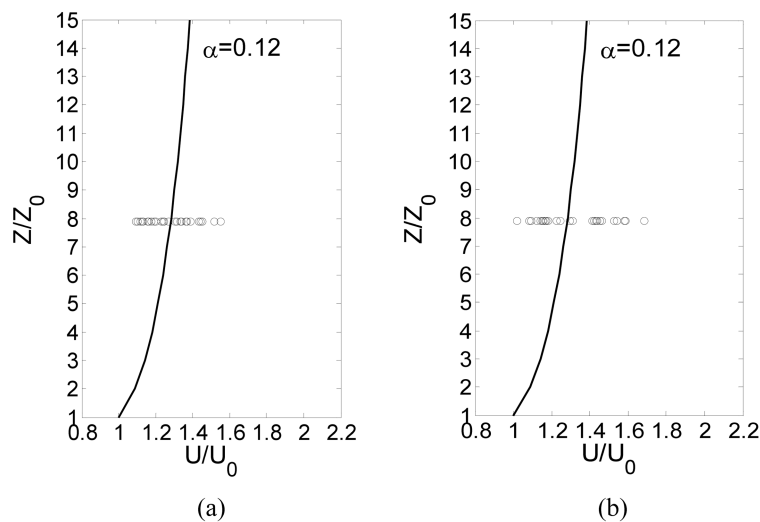

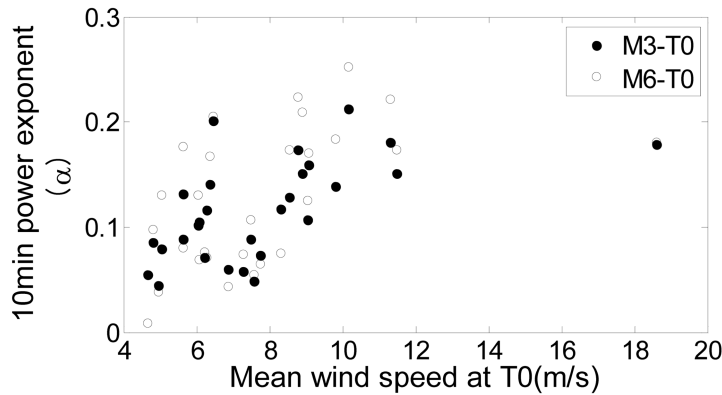Fig. 10 The mean wind profile at bridge deck (a) M3 and (b) M6

Fig. 11 The relationship between mean wind speed of upstream and power exponent

that the 10-min power exponent increases with increase in 10-min mean wind speed.

3.3 Turbulence intensity

The turbulence intensity represents the intensity of the fluctuation of wind speed. The longitudinal, lateral and vertical turbulence intensities are determined by the following equations

$$I_u = \frac{\sigma_u}{U} \quad I_u = \frac{\sigma_v}{U} \quad I_w = \frac{\sigma_w}{U} \tag{5}$$

Where σ_u, σ_v, σ_w are the standard deviations of the fluctuation components of wind velocity in corresponding directions.

Fig. 12 describes the variations of 10-min turbulent intensity with time at upstream of M3 and M6. The average turbulence intensities are 15.0, 13.1 and 9.1% for longitudinal, lateral and vertical fluctuating wind velocity at upstream of M3, respectively and the ratio of the three components is 1:0.87:0.70. At upstream of M6, the average turbulence intensities are 14.8, 13.5 and 9.5% for longitudinal, lateral and vertical fluctuating wind velocity, respectively, and the ratio of the three components is 1:0.91:0.64. Although the turbulence intensities at M3 and M6 are not completely identical, the corresponding average values of the three components at M3 and M6 are very close to each other.

Fig. 13 shows the relationship between 10-min turbulent intensity and mean wind speed. In the low wind speed range, the turbulent intensity decreases with the mean wind speed increase, however, in the higher wind speed region, there is not distinct tendency for turbulent intensity with the mean wind speed.

Fig. 14 presents the variations of standard deviation of longitudinal, lateral and vertical fluctuant wind velocity with mean wind speed. It can be observed that the standard deviation increases with the increase in mean wind speed.

The relationship shown in Figs. 13 and 14 for M3 and M6 is almost identical.

3.4 The power spectral density of fluctuating wind velocity and turbulence integral scale

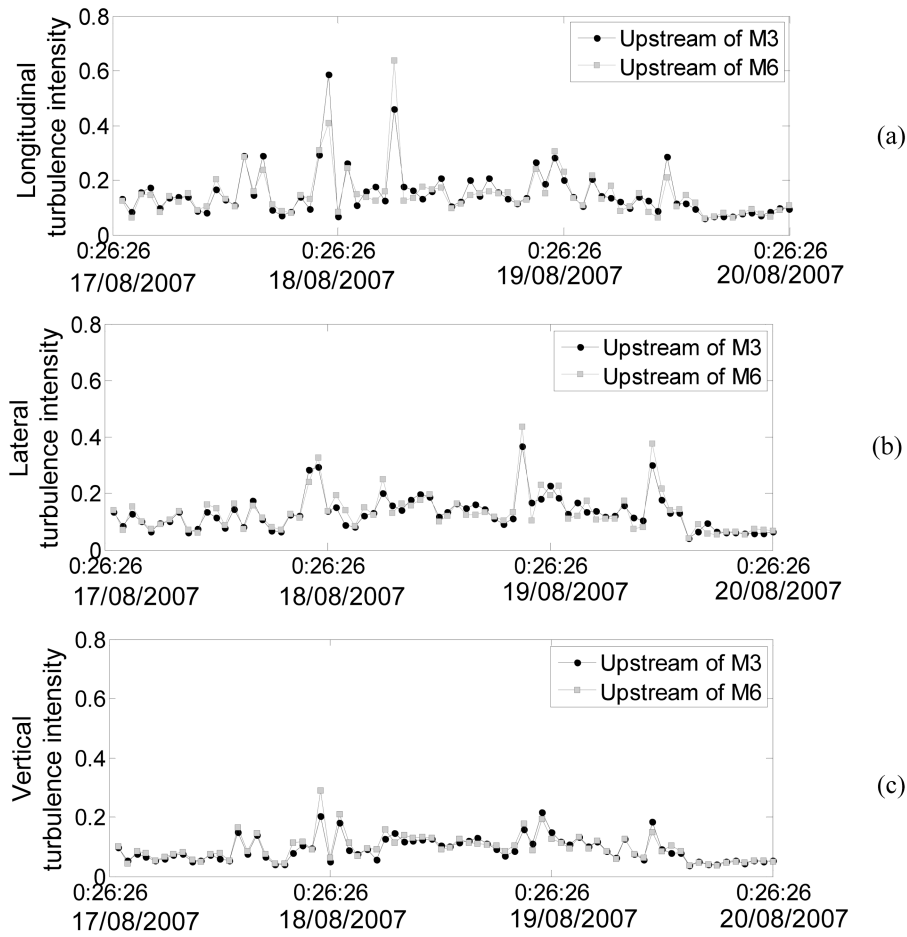The power spectral density represents the energy distribution of fluctuating wind in frequency

Fig. 12 Variations of 10-min turbulent intensity with time at upstream of M3 and M6 (a) longitudinal, (b) lateral and (c) vertical

domain. It is a key parameter to estimate the buffeting response of long-span bridges.

Usually, Von Karman spectra is a suitable representation of wind velocity auto-power spectra and has the following form (Fu *et al.* 2008)

$$
\left\{
\begin{array}{l}
\dfrac{S_u(f)}{\sigma_u^2} = \dfrac{4L_u/U}{[1 + 70.8(L_uf/U)^2]^{5/6}} \\[4mm]
\dfrac{S_\varepsilon(f)}{\sigma_\varepsilon^2} = \dfrac{4L_\varepsilon/U[1 + 755.2(L_\varepsilon f/U)^2]}{[1 + 283.2(L_\varepsilon f/U)^2]^{11/6}} \quad (\varepsilon = v, w)
\end{array}
\right.
\tag{6}
$$

where f is the frequency, S_u, S_v, S_w are longitudinal, lateral and vertical power spectral densities, L_u, L_v, L_w are the estimated turbulence integral scales along three directions.
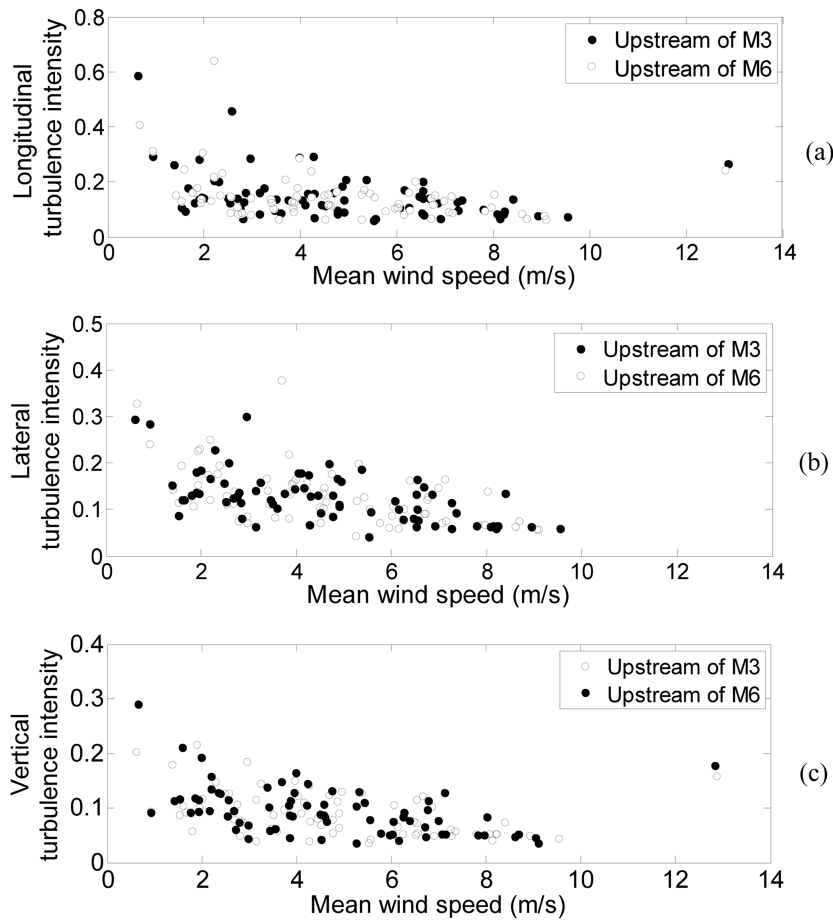
Fig. 13 The relationship of turbulence intensity and mean wind at upstream of M3 and M6 (a) longitudinal, (b) lateral and (c) vertical

Fig. 15 shows the normalized spectra of fluctuant wind velocity at upstream of M6 and M3, respectively. In the spectral analysis, Welch's averaged periodogram method is used to estimate the auto power spectral. Hamming window is employed to filter noise. 10 minutes (6:36:27-6:46:26, 17/08/2007) wind speed time history is categorized into 9 segments, and the overlapped length is 1 min between two neighbor segments. The PSD estimated by the Von Karman spectrum is also presented in this figure. It is seen that both the PSD of the measured wind velocities at upstream of M3 and M6 are well fitted with the Von Karman spectrum in the range of [0.1 10] Hz. However, in range of [0 0.1] Hz, both the PSDs of the measured wind velocities at upstream of M3 and M6 are slightly deviated from the Von Karman spectrum. It possibly attributes to the coherence structures of nature wind.

The turbulence integral scale is defined as the average eddy scale of turbulence wind. In this study, the turbulent integral scale is estimated from the auto power spectra of measured wind speed with the Von Karman spectrum formula. The nonlinear fitting is conducted based on Eq. (5) to obtain the turbulent integral length L_u, L_v, L_w and the results are shown in Fig. 16. For the upstream
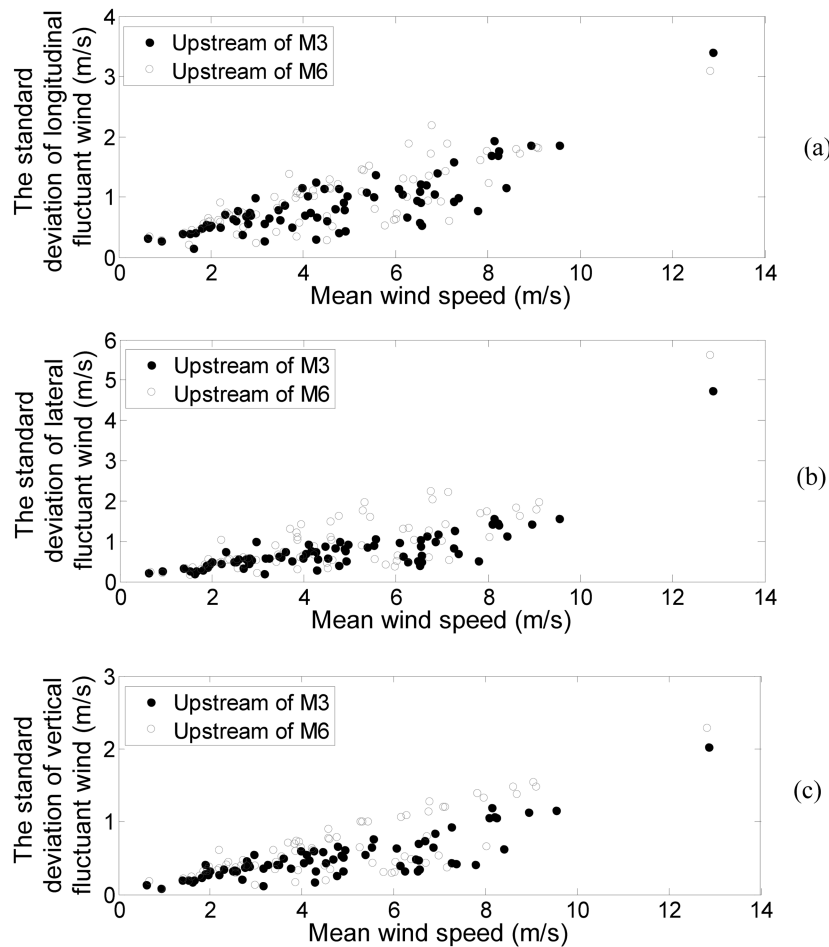
Fig. 14 The relationship between standard deviation of fluctuant wind speed and 10-min mean wind speed (a) longitudinal, (b) lateral and (c) vertical

of M3, the mean values of longitudinal, lateral and vertical turbulence integral lengths are 59.2, 46.4 and 25.4 m, respectively. The ratio of these three components is 1:0.78:0.43. For the upstream of M6, the mean values of longitudinal, lateral and vertical turbulence integral lengths are 58.1, 44.6 and 26.2 m, respectively. The ratio of these three components is 1:0.77:0.44. It is worth noting that the turbulence integral scales at these two sections are very similar. The relationship between turbulence integral scale and mean wind speed shown in Fig. 17 indicates that, for the longitudinal and lateral turbulence integral lengths, there is obvious increase tendency with increase in the mean wind speed, however, for the vertical turbulence integral scale, it almost keeps constant.

3.5 Coherence of the wind

The coherence function represents the relationship of two time series in frequency. It is a critical factor to estimate the buffeting response of long-span bridges and defined as
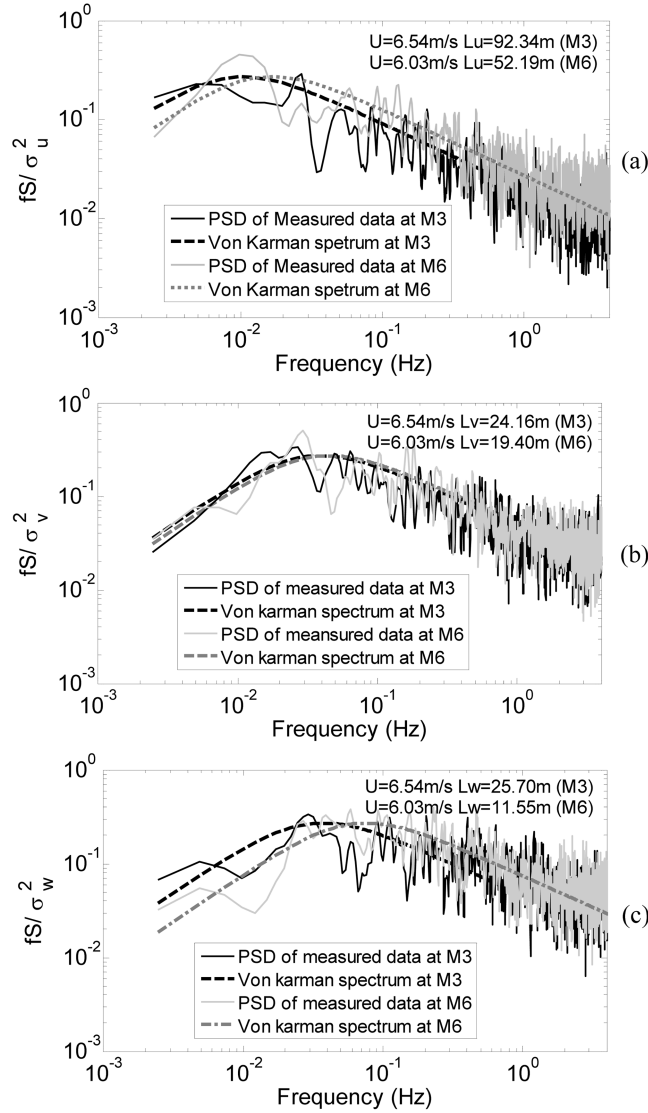
Fig. 15 10-min power spectrum density of fluctuant wind speed at upstream of M6 (a) longitudinal, (b) lateral and (c) vertical

$$C_{xy} = \frac{|S_{xy}|^2}{S_{xx}S_{yy}} \tag{7}$$

where C_{xy} is the coherence function, S_{xy} is the crossing power density spectrum, and S_{xx}, S_{yy} are auto-power density spectrum.

The coherence function of the three components of fluctuating wind at M3 upstream and M6 upstream are shown in Figs. 18 and 19, respectively. The curves indicate that most of the coherence coefficients are very small, implying that the three components of fluctuating wind have very low correlation in frequency. Therefore, the cross power density spectrum of different directions can be
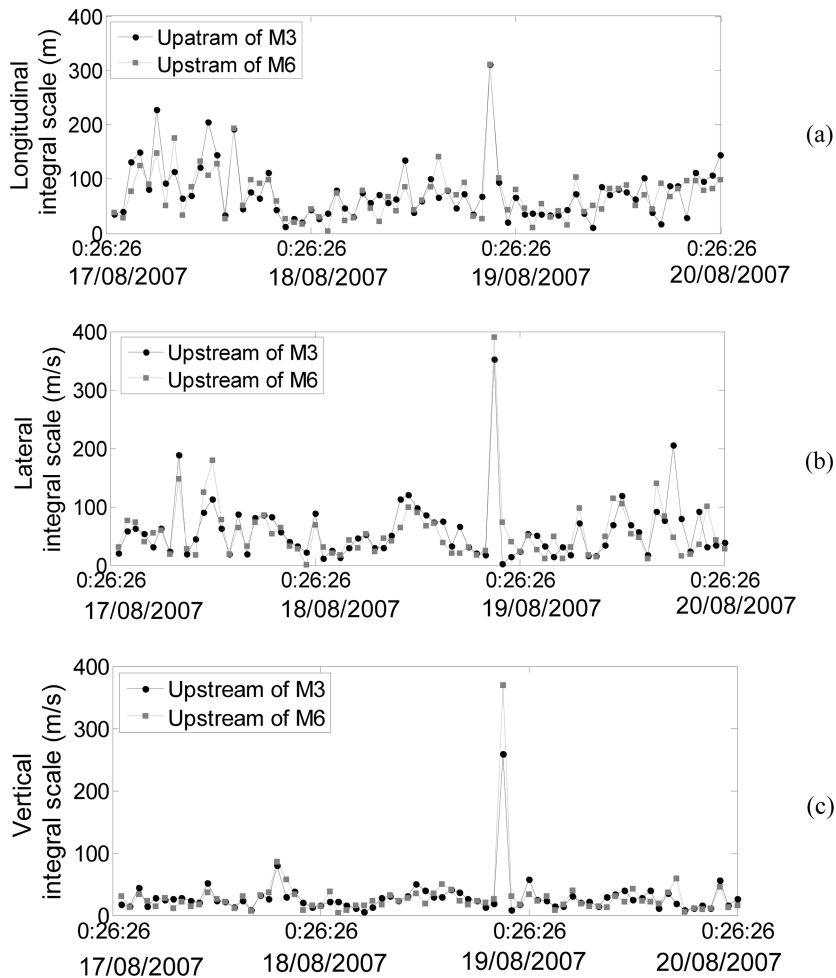
Fig. 16 10-min turbulence integral scale at upstream of M3 and M6 (a) longitudinal, (b) lateral and (c) vertical

neglected for the analysis of the buffeting response of this bridge. Although the coherence functions for M3 and M6 are not completely identical, the same phenomenon may be observed.

The coherence function of the fluctuating wind along the bridge is frequently used to calculate the buffeting response. The coherence function between M3 upstream and M6 upstream (about 150 m apart from each other) shown in Fig. 20 indicates that the coherence coefficients are very small. As analysis above, the longitudinal integral scale length at the two sections are 59.2 and 58.1 m, which are smaller than their distance. Hence, their correlation is very weak.

4. The non-stationary characteristics of fluctuating wind

Recently, the nature wind is regarded as a non-stationary random process because of its special characteristics, such as cohere structures, intermittence and etc. The non-stationary characteristics
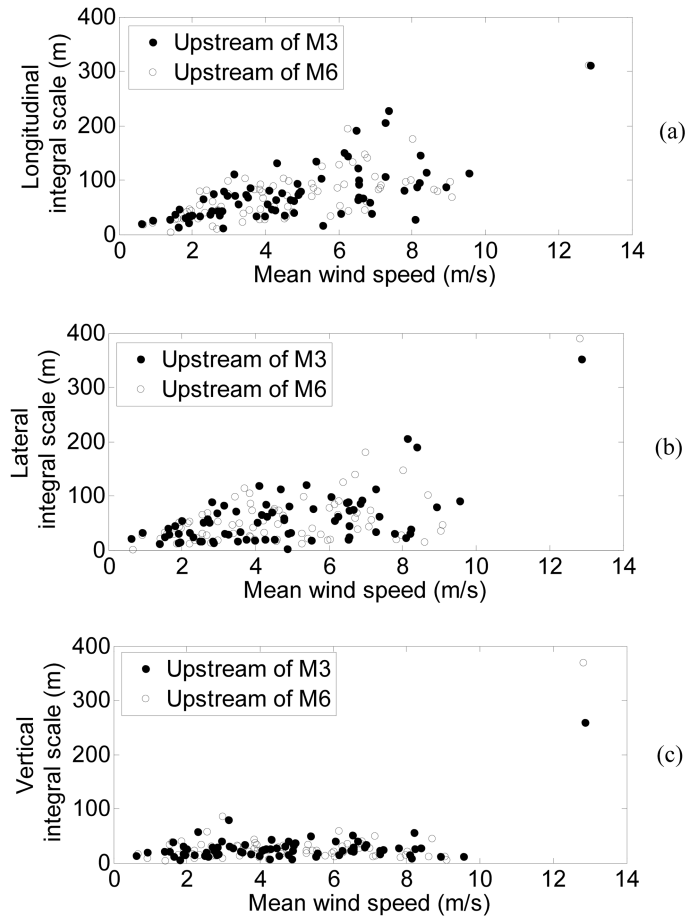
Fig. 17 The relationship between turbulence integral scale and mean wind speed (a) longitudinal, (b) lateral and (c) vertical
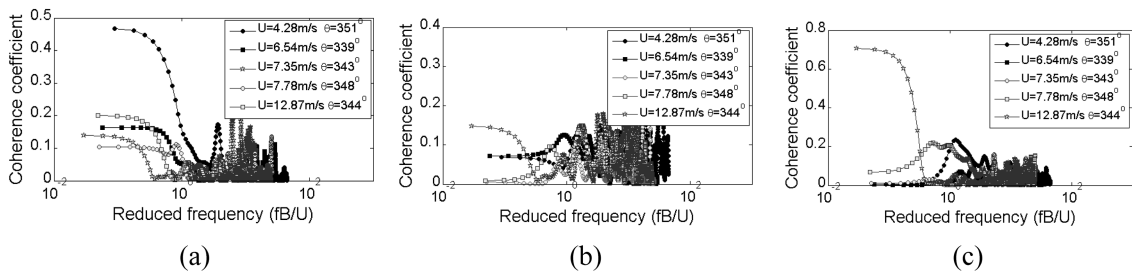

Fig. 18 The coherent function of the three components of wind at upstream of M3 (a) *uv*, (b) *uw* and (c) *vw*

may play very important roles in the buffeting response of bridges. For analysis of non-stationary characteristics, wavelet transform is a powerful tool (Hajj *et al.* 1998, Dunyak *et al.* 1998, Terradellas *et al.* 2001, Kareem and Kijewski 2002, Boldes *et al.* 2003, Chabalko *et al.* 2005).
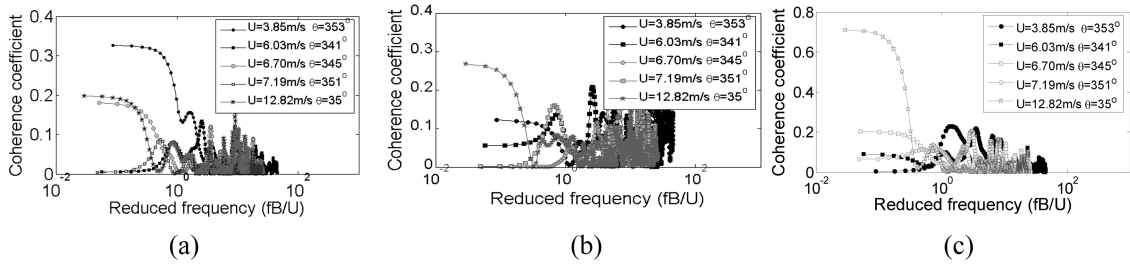
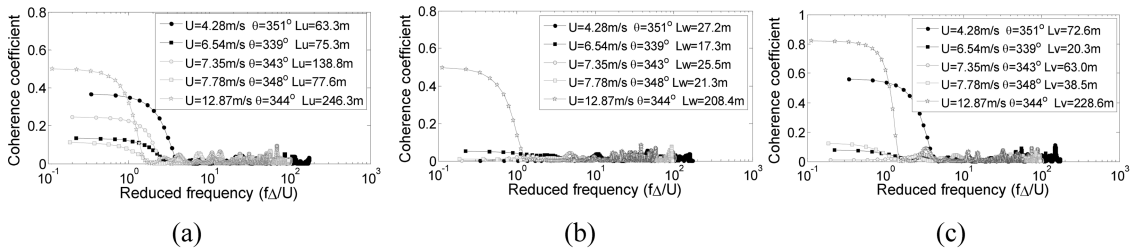Fig. 19 The coherent function of the three components of wind at upstream of M6 (a) *uv*, (b) *uw* and (c) *vw*

Fig. 20 The coherent function between upstream of M3 and M6 (a) *uu'*, (b) *vv'* and (c) *ww'*

4.1 The continuous wavelet transform

The continuous wavelet transform, $W(a,t)$, is defined as

$$W(a, t) = a^{-\frac{1}{2}} \int_{-\infty}^{+\infty} f(\tau) \psi^* \left(\frac{t - \tau}{a} \right) d\tau \qquad (8)$$

where $f(\tau)$ is a signal, $\psi(a,t)$ is the wavelet function, ψ^* denotes the complex conjugate of ψ, a is the scale and t denotes the time.

A number of functions can be candidates as wavelet function. In the paper, DB4 is selected as the wavelet function and depicted in Fig. 21. The scale-frequency relationship for the DB4 wavelet transform is
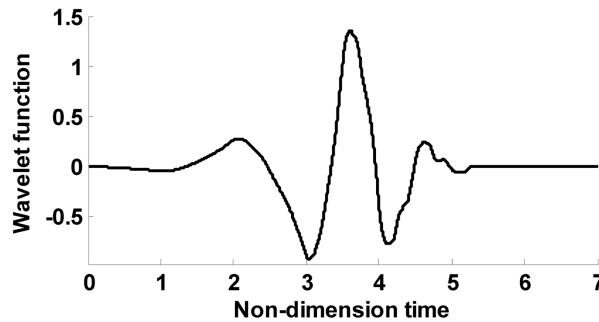

Fig. 21 DB4 wavelet function

$$f = \frac{0.731 f_s}{a} \qquad (9)$$

where *f* is the frequency corresponding to scale *a*, and f_s is the sampling frequency. In this paper, the sampling frequency of wind is 10 Hz.

4.2 The time-scale characteristic of the fluctuating wind speed

Fig. 22 (left) shows the contour plot of the square wavelet coefficients for fluctuant wind velocity at upstream of M3. For the longitudinal fluctuant wind, the large scale fluctuations appear at *t*=45-55s, $\log_2 a$=8-9, the peak is *t*=88s and $\log_2 a$=8.30 (*f*=0.0234 Hz). For the lateral fluctuant wind, the large scale fluctuations appear *t*=10-20s, $\log_2 a$=8-9, the peak is *t*=36s, $\log_2 a$=8.81 (*f*=0.0162 Hz),
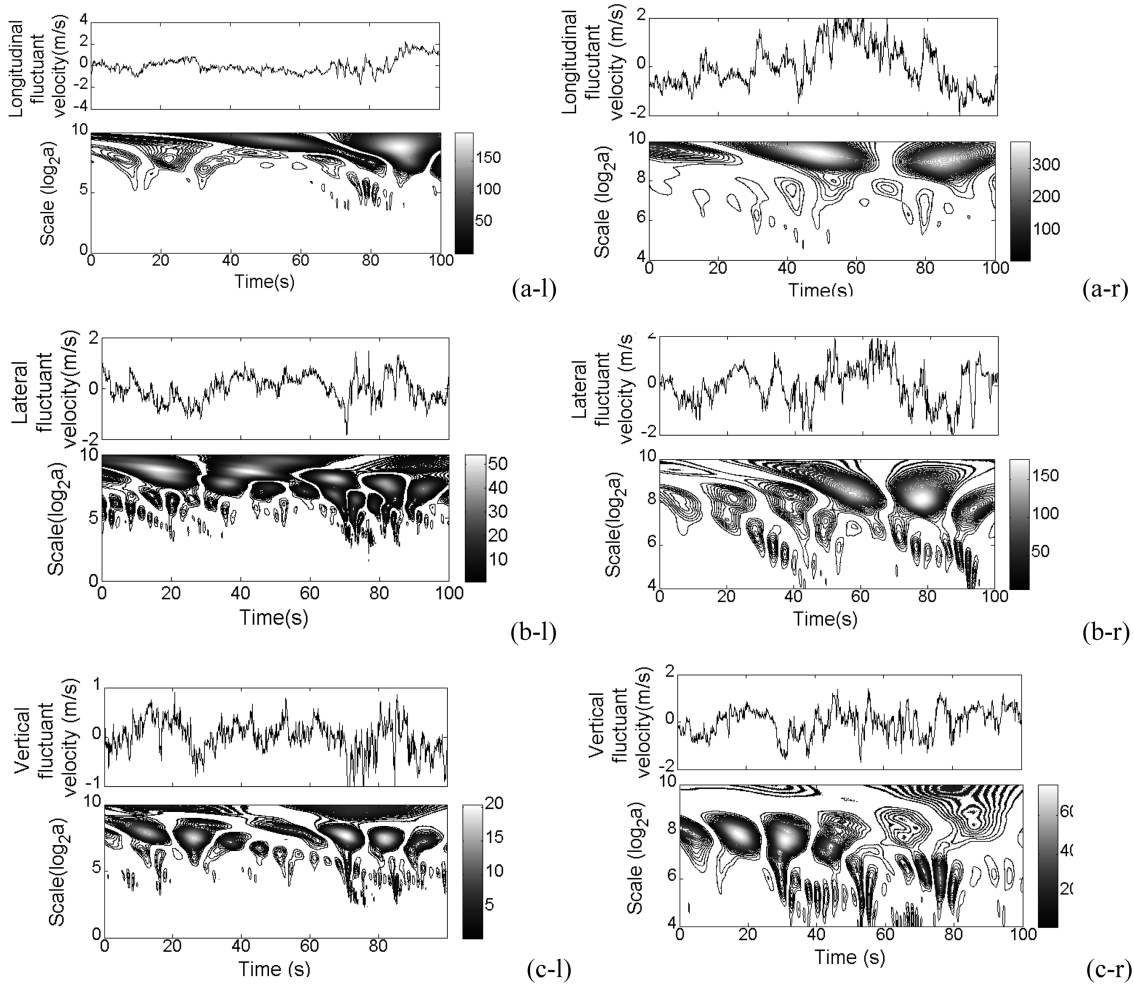

Fig. 22 Contour plots of the square wavelet coefficients of fluctuant wind at upstream of M3 (left) and M6 (right) (a) longitudinal, (b) lateral and (c) vertical

t=52-61s, log$_2 a$=8-9, and the peak is t=58s, log$_2 a$=8.64 (f=0.0180 Hz). For the vertical fluctuant wind, the large scale fluctuations appear t=12-22s, log$_2 a$ =7-8 and the peak is t=17s, log$_2 a$ =7.64 (f=0.0363 Hz), t=80-84s, log$_2 a$ =7-8 and the peak is t=492s, log$_2 a$ =7.47 (f=0.0414 Hz).

Fig. 22 (right) shows the contour plot of the square wavelet coefficients for fluctuant wind velocity at upstream of M6. For the longitudinal fluctuant wind, the large scale fluctuations appear at t=25-35s, log$_2 a$ =9-10, the peak is t=30s and log$_2 a$ =9.4 (f=0.012 Hz), t=45-55s, log$_2 a$=9-10 and the peak is t=50s and log$_2 a$=9.6 (f=0.0132 Hz). For the lateral fluctuant wind, the large scale fluctuations appear t=52-62s, log$_2 a$=8-9, the peak is t=58s, log$_2 a$ =8.44 (f=0.0228 Hz); t=74-64s, log$_2 a$=8-9, and the peak is t=78s, log$_2 a$=8.18 (f=0.0276 Hz). For the vertical fluctuant wind, the large scale fluctuations appear t=12-22s, log$_2 a$=7-8 and the peak is t=17s, log$_2 a$=7.88 (f=0.0342 Hz), t=26-36s, log$_2 a$=7-8 and the peak is t=31s, log$_2 a$ =7.69 (f=0.0396 Hz).

The above results indicate that a) The distribution of wavelet coefficients is irregular in time-scale plane and the peaks show high intermittent. b) The peaks with large values almost distribute in the large scale zone, all larger than 128, i.e., large scales carry the most of energy of the fluctuating wind (the square of wavelet coefficients represent the energy distribution). c) In small scale zone, rare peaks with large values occur, implying low energy in small scale zone. d) The large scale fluctuations of fluctuating wind velocity contain great energy. It seems reasonable to hold that the structures corresponding to peaks are the coherent structures and they are adjacent. These special structures can give an interpretation that the PSD of nature wind deviates from the Von Karman spectrum in the low frequency domain. f) In the large scale zone, the appearance time of the special structures for M3 and M6 is different and the corresponding frequency with the structure is also different, i.e., the time-frequency features of the wind at M3 and M6 are different.

The characteristics in small scale zone are also analyzed here because they are related with buffeting response of long-span bridges. To obtain the fine structures of fluctuant wind velocity in time-frequency domain, the longitudinal fluctuant wind velocities at M3 and M6 are categorized into 3 segments in frequency domain with band-pass filter method, i.e. the frequency bands are [0.3175~0.625 Hz], [0.625~1.25 Hz] and [1.25~2.5 Hz]. The contour plots of square wavelet coefficients of filtered longitudinal fluctuant wind velocity at M3 (left) and M6 (right) are shown in Fig. 23. It can be observed that the high energies all distribute in [70~80s] for three directions at M3, while in [50~70s] at M6. The more interesting finding is that the strong coherence structures also appear in these durations, in other words, the distributions of energy in time have self-similarity.

4.3 The time-frequency coherence of the wind between M3 and M6 upstream

The spatial correlation of the wind between M3 and M6 upstream has been analyzed using FFT and the coherence coefficients are very small (most of them below 0.20). However, this method cannot give the temporal information of the wind in time-frequency domain. Usually, the nature wind is a non-stationary process and should be described using time-frequency signal process approaches. Therefore, a spatial correlation in the time-frequency (Gurley *et al.* 2003) is adopted herein to solve this problem. The wavelet coherence is defined as

$$\left[C^W(a, t)\right]^2 = \frac{\left|S_{xy}^W(a, t)\right|^2}{S_{xx}^W(a, t)S_{yy}^W(a, t)} \tag{10}$$

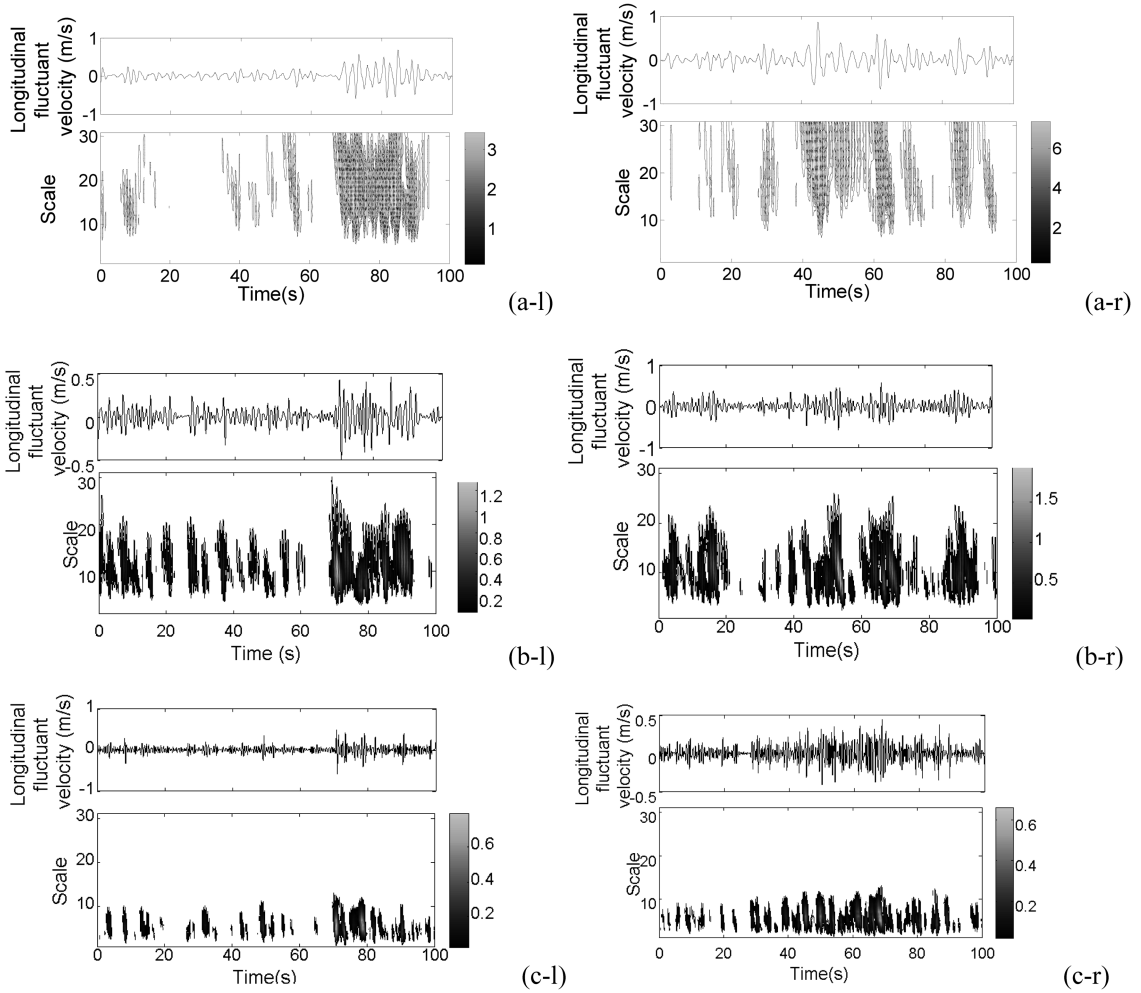where the localized power spectra are given by

Fig. 23 Contour plots of the square wavelet coefficients of filtered longitudinal fluctuant wind at upstream of M3 (left) and M6 (right) (a) [0.3175~0.625Hz], (b) [0.625~1.25Hz] and (c) [1.25~2.5Hz]

$$S_{ij}^{W}(a, t) = \int_{T} W_{i}^{*}(a, t) W_{j}(a, t) d\tau \qquad (11)$$

In the study, the time integration window of $T=[t-60s, t+60s]$ is selected and DB4 is still be used as the wavelet function.

Fig. 24 shows the time-scale coherence function between M3 and M6 upstream. The 3-D plots present that the coherence coefficients are not uniform along time axis, in some durations, they show stronger correlation, however, in other durations, they are very weak in correlation. Hence, it has intermittent characteristic. In addition, the correlation in low frequency range is strong for longitudinal and lateral wind speeds, for vertical wind speed, the correlation seems strong within all frequency range.
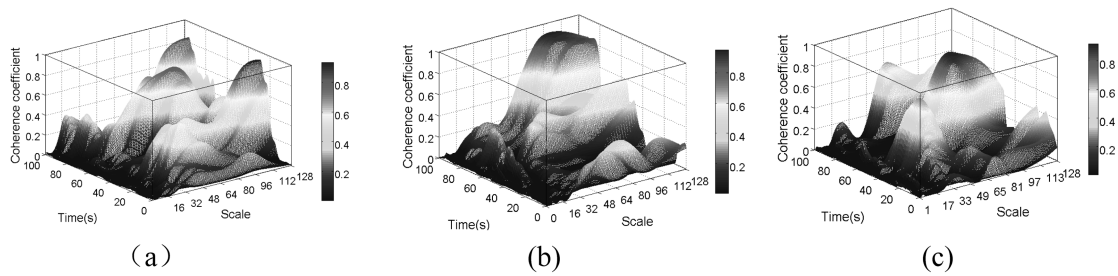
Fig. 24 The time-frequency coherence function between upstream of M3 and M6 (a) *uu'*, (b) *vv'* and (c) *ww'*

5. The flow characteristics around the bridge deck

5.1 The change in mean wind speed in wake-flow of deck (bluff body)

The anemometers at wake-flow of deck may measure the interfered wind speed, associated with the deck (bluff body).

Fig. 25 shows the 10-min mean wind speed in the inflow (upstream) and wake-flow at M3 and M6. The average mean wind speeds are respectively 4.70 and 3.27 m/s for inflow and wake-flow at M3, and 4.65 and 3.43 m/s at M6. After inflow passes through the bridge deck at M3, the mean wind speed reduces by 30.3%, i.e., $U_{wake-flow}=0.7U_{inflow}$. While, at the section of M6, the mean wind speed reduces by 26.2%.

The relationship of the decrement of 10-min mean wind speed between inflow and wake-flow with mean wind speed of inflow is shown in Fig. 26. The decrement of mean wind speed increases with the increase in mean wind speed of inflow.

5.2 The fluctuating characteristics of wake-flow

Figs. 27 and 28 show 10-min (6:36:27-6:46:26, 17/08/2009) fluctuating wind velocities in the wake-flow at M3 and M6. The results in Fig. 29 are the turbulence intensities of the wind velocity. The average turbulence intensities for the longitudinal, lateral and vertical fluctuating wind velocity at M3 are 33.1, 28.1 and 18.8%, respectively and the ratio of the three components is 1:0.85:0.57
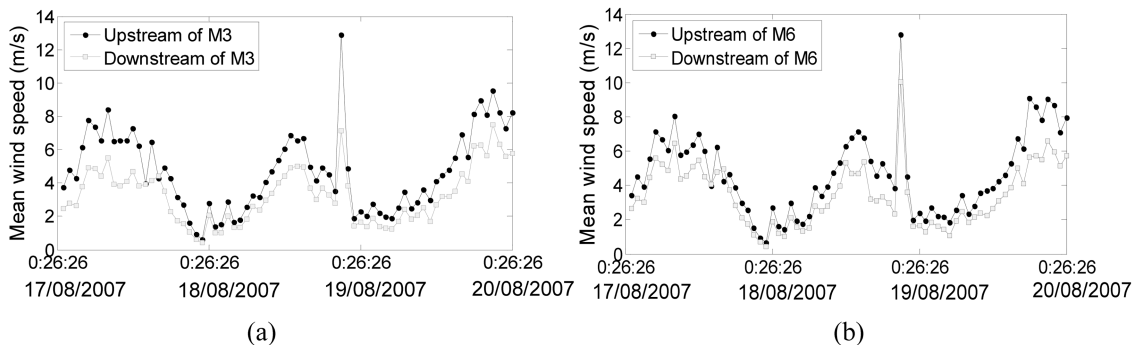

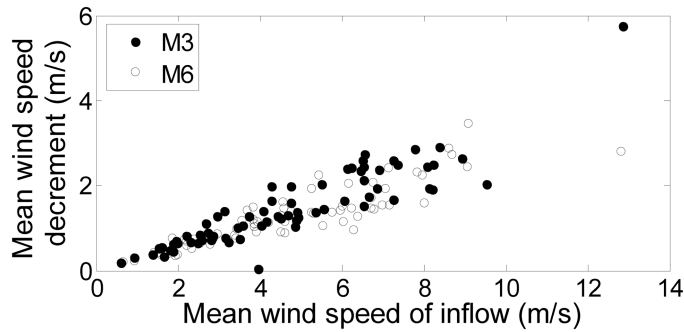Fig. 25 10-min mean wind speed in inflow and wake-flow at (a) M6 and (b) M3

Fig. 26 Relationship of decrement of 10-min mean wind speed between inflow and wake-flow with inflow mean wind speed
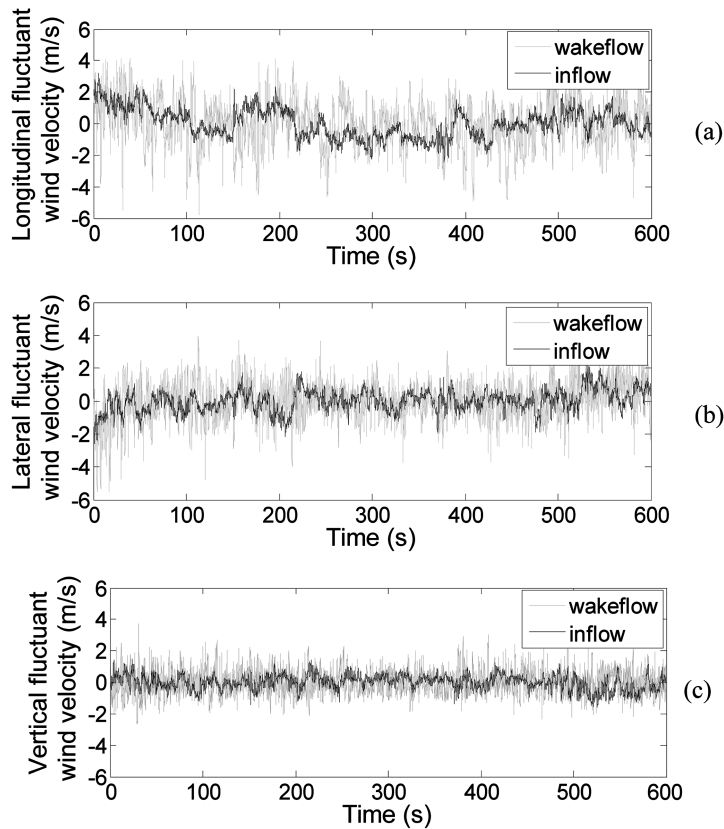

Fig. 27 10-min fluctuant wind velocity of wake-flow at M3 (6:36:27-6:46:26, 17/08/2007) (a) longitudinal, (b) lateral and (c) vertical

(which are 15.0, 13.1 and 9.1% for inflow at M3). While at M6, they are 36.4, 33.9 and 22.9% for the longitudinal, lateral and vertical turbulence intensities, respectively and the ratio is 1:0.93:0.63 (which are 14.8, 13.5 and 9.5% for inflow at M6). It is readily seen that the turbulence intensities of wake-flow are much greater than those of inflow. Fig. 30 presents the relationship between standard
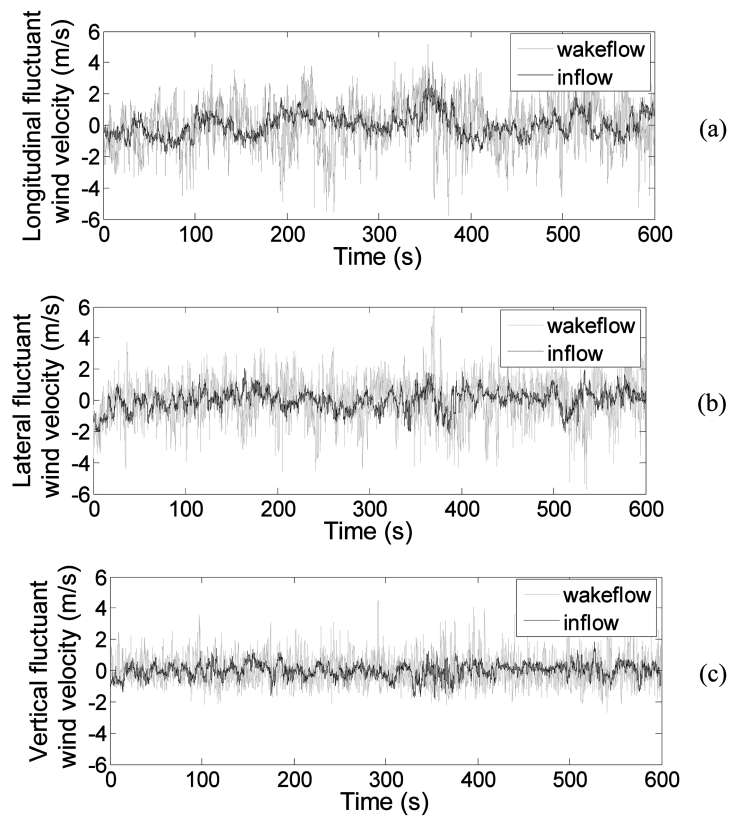
Fig. 28 10-min fluctuating wind velocity of wake-flow at M6 (6:36:27-6:46:26, 17/08/2007) (a) longitudinal, (b) lateral and (c) vertical
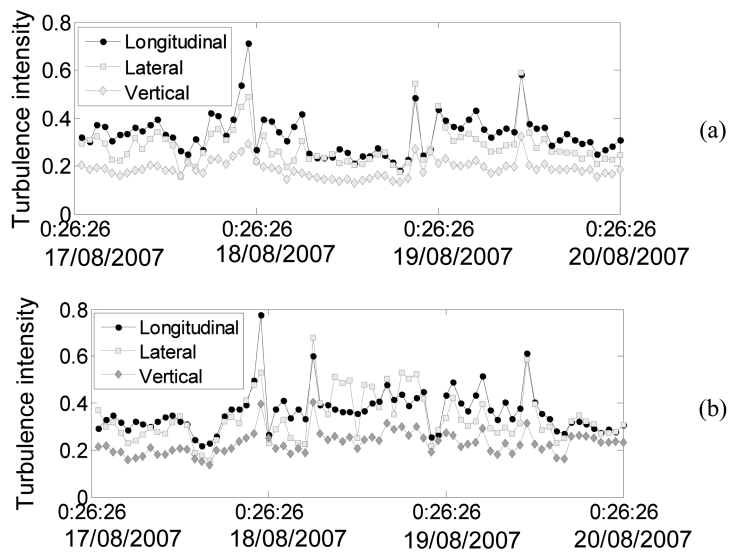
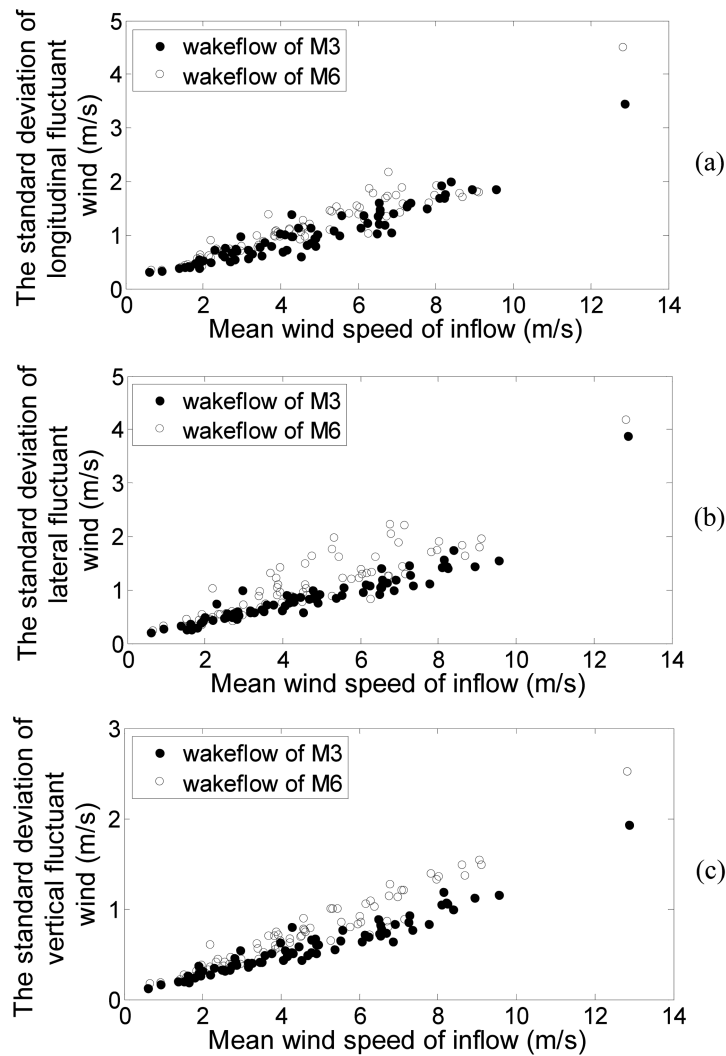Fig. 29 10-min turbulence intensity of wake-flow at (a) M3 and (b) M6

Fig. 30 The standard deviation of fluctuant wind in wake-flow with mean wind speed of inflow (a) longitudinal,
      (b) lateral and (c) vertical

deviations of fluctuating wind in wake-flow and mean wind speed of inflow. The standard deviations of fluctuating wind in wake-flow approximately linearly increase with increase in mean wind speed of inflow. The relationship of the mean wind speed of inflow, the RMSs of inflow and wake-flow, as shown in Fig. 31 presents that the mean wind speed of inflow is an important factor for fluctuation of wake-flow. In addition, RMS of inflow also has strong positive impact on the fluctuation of wake-flow.

   Fig. 32 shows the 10-min power spectral densities of wake flow at M6 and M3, and their fitted Von Karman spectrums. In general, as those of inflow, the PSDs of measured fluctuating wind velocity of wake-flow fit well with Von Karman spectrum. However, as shown in Fig. 32, in the range of [0, 0.5] Hz, there also exits slight deviation between PSD of measured fluctuant wind and Von Karman spectrum. From the PSDs of measured fluctuant wind, it can be seen that there are
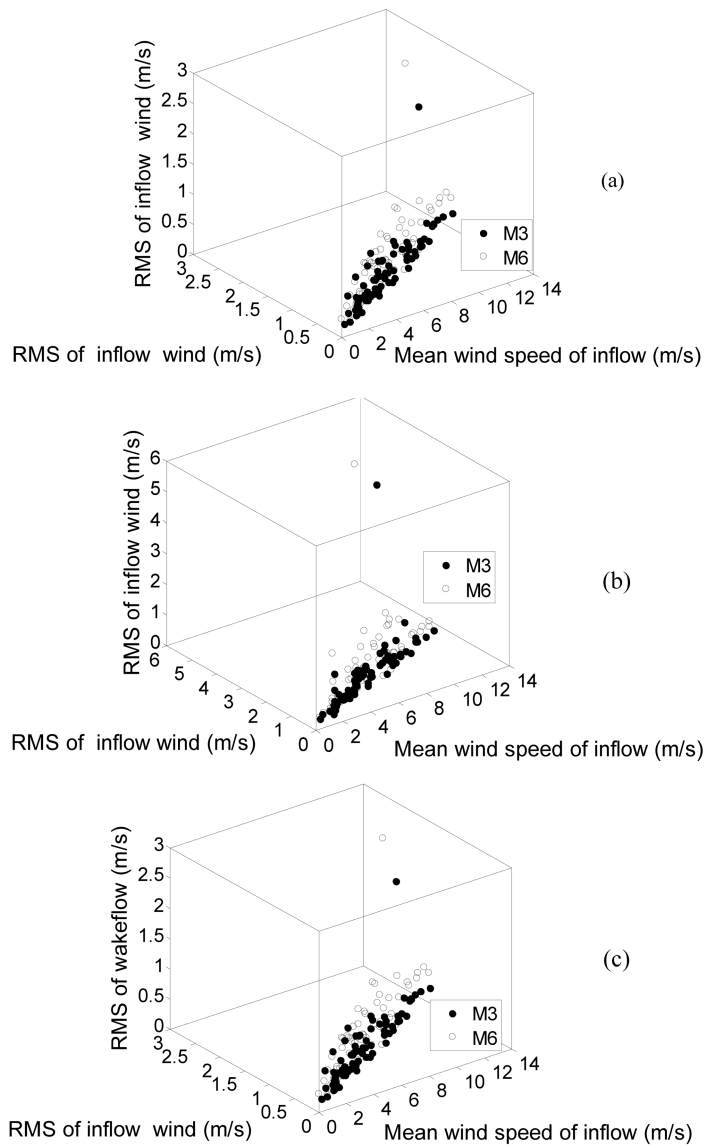
Fig. 31 The relationship of the mean wind speed of inflow, the RMS of inflow and the RMS of wake-flow
fluctuating velocity (a) longitudinal, (b) lateral and (c) vertical

some characteristic frequencies, although the energy is not very large.

The 10-min turbulence integral scale of the wake-flow, obtained through the Von Karman spectrum, is presented in Fig. 33. The average values of turbulence integral length of the longitudinal, lateral and vertical fluctuating wind velocity at M3 are 11.8, 7.7 and 2.0 m (which are 59.2, 46.4 and 25.4 m for inflow at M3), respectively. The ratio of the three components is 1:0.0.65:0.17. At M6, the values are 9.3, 8.7 and 2.6 m (which are 58.1, 44.6 and 26.2 m for inflow at M6), and the ratio of the three components is 1:0.93:0.30. The relationship between turbulence integral scale and mean wind speed of wake-flow is shown in Fig. 34. The distribution of
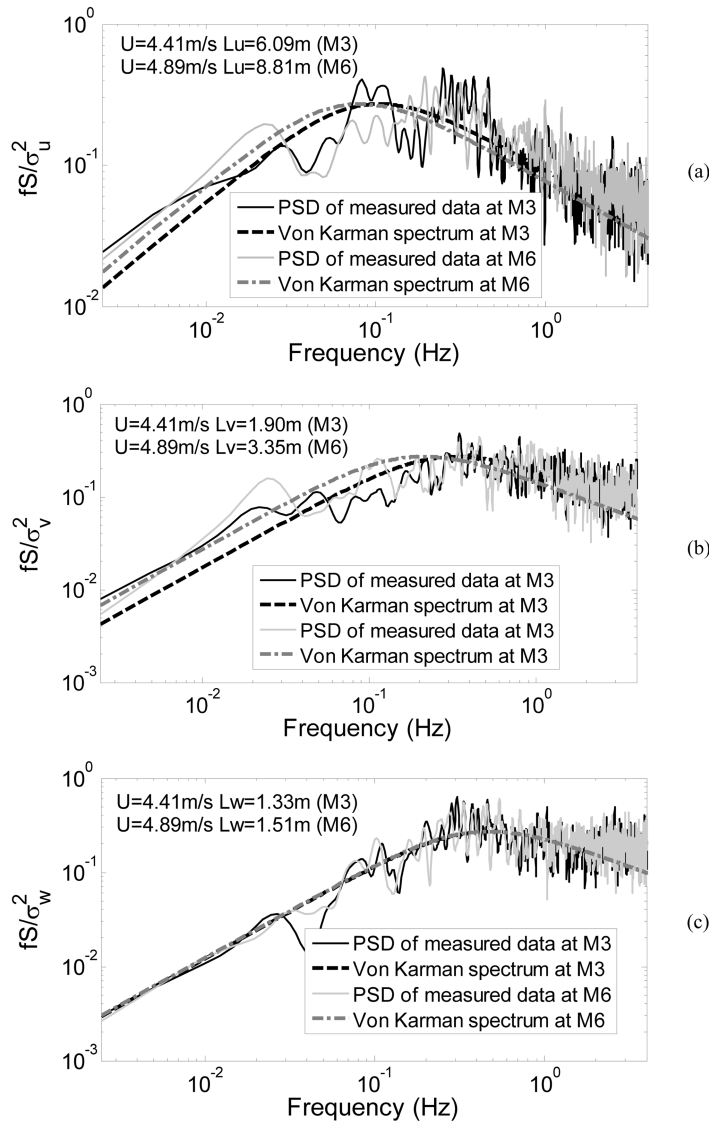
Fig. 32 10-min power spectral density of wake-flow at M6 and M3 (a) longitudinal, (b) lateral and (c) vertical

turbulence integral lengths are scatter, there is not obvious tendency to increase with the increase in mean wind speed. Comparing with the turbulence integral lengths of inflow, it is found that the turbulence integral scales decrease rapidly when the wind passing through the bridge deck, and the turbulence integral scale does not increase with the mean wind speed changes.

5.3 The time-frequency characteristics of wake-flow

The wavelet transform method, DB4 as wavelet function, is used to analyze the time-frequency characteristics of the wake-flow. Fig. 35 shows the contour plots of square wavelet coefficients of the fluctuating wind velocity in the wake-flow at M3 (left) and M6 (right). Large fluctuations in
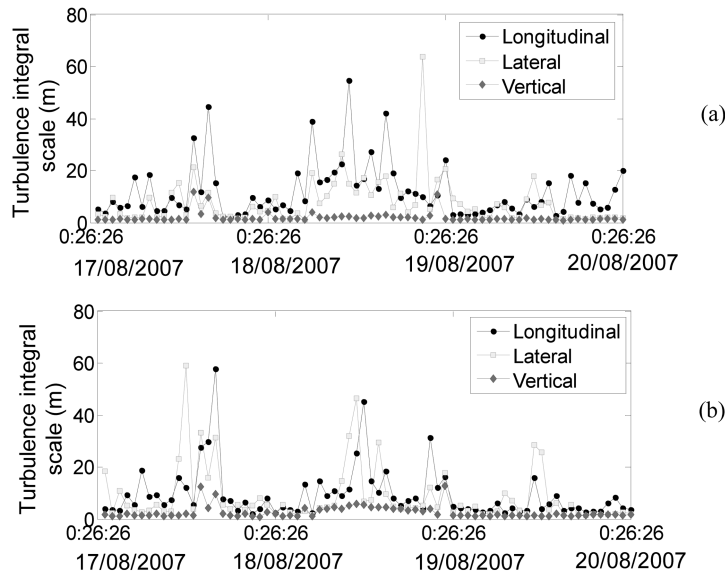
Fig. 33 10-min turbulence integral scale at downstream of (a) M3 and (b) M6

each fluctuating wind component can be observed. For the wake-flow at M3, the peaks are as follows: for the longitudinal fluctuating wind, the peaks appears at (t=70s, $\log_2 a$=7.97, f=0.030 Hz) and (t=85s, $\log_2 a$=7.73, f=0.036 Hz); for the lateral fluctuating wind, the peaks occur at (t=68s, $\log_2 a$=7.59, f=0.036 Hz); for the vertical fluctuating wind, peaks form at (t=78s, $\log_2 a$=5.13, f=0.21 Hz) and (t=80s, $\log_2 a$=4.46, f=0.330 Hz). For the wake-flow at M6, the peaks are as follows: for the longitudinal fluctuating wind, the peaks appear at (t=61s, $\log_2 a$=7.05, f=0.552 Hz) and (t=68s, $\log_2 a$=6.67, f=0.072 Hz); for the lateral fluctuating wind, the peaks occur at (t=68s, $\log_2 a$=6.23, f=0.096 Hz) and (t=72s, $\log_2 a$=6.13, f=0.102 Hz); for the vertical fluctuating wind, peaks form at (t=61s, $\log_2 a$=6.85, f=0.066 Hz) and (t=68s, $\log_2 a$=6.67, f=0.072 Hz).

Comparing the wavelet scalograms of fluctuant wind in inflow and wake-flow, it can be observed that the scales of coherence structures in wake-flow are much smaller than that in inflow, and their correlation in time-frequency domain is very small. It indicates that the fluctuation of inflow is not a critical factor to form the fluctuant characteristics of wake-flow. In fact, the formation of wake-flow is associated with vortex shedding when the mean wind speed passing through the bridge deck. The wavelet scalogram of wake-flow indicates the evolution of turbulence in time-frequency domain. The coherence structure presents the large vortex growth and the corresponding frequency indicates vortex pulsation frequency. In small scale zones, the peaks present small vortex development.

Comparing the wavelet scalograms of fluctuant wind at M3 and M6 wake-flow, it is found that the evolution of turbulence in time-frequency domain at these two positions are different, i.e., along the bridge, the flow characteristics around bridge deck do not keep identical.

6. Conclusions

This paper investigates the correlations of wind observed on an actual bridge. Some conclusions are summarized as follows:
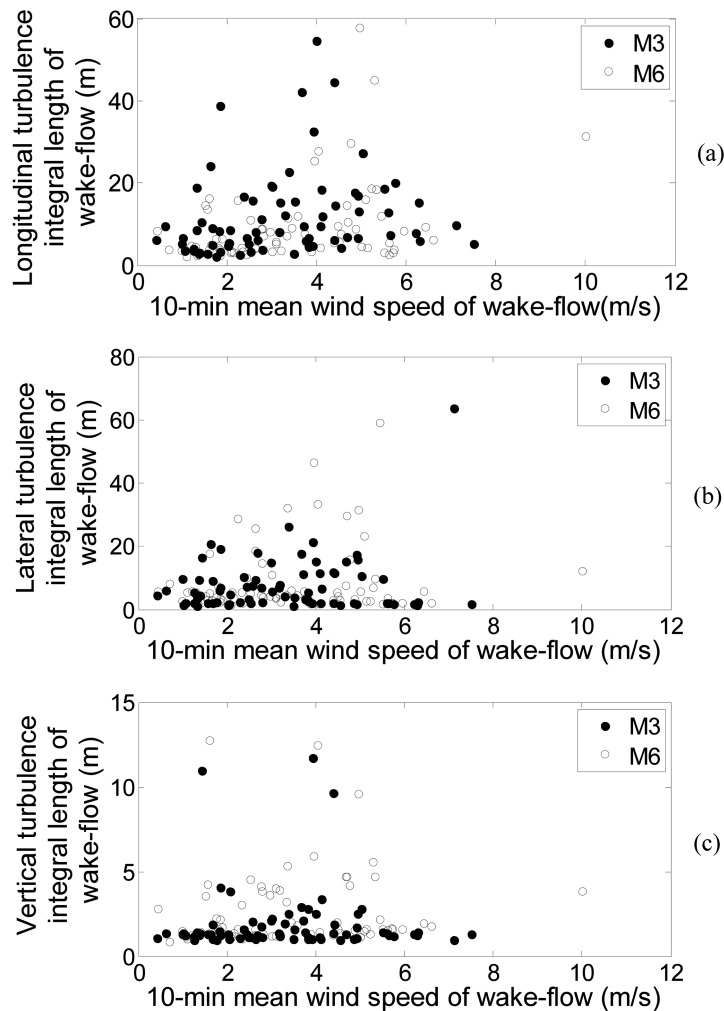
Fig. 34 The relationship between turbulence integral scale and mean wind speed of wake-flow (a) longitudinal, (b) lateral and (c) vertical

(1) The wind has the same characteristics in mean wind speed and wind direction at upstream along the bridge length. The average turbulence intensities and turbulence integral lengths at upstream of two locations along the bridge axis are very close.

(2) In general, the Von Karman spectrum is fitted well with the PSD of the nature wind at upstream of two locations. However, in the low frequency domain for the two positions, the PSDs of the measured wind velocities are slightly deviated from the Von Karman spectrum.

(3) Spatial correlation of the fluctuant wind between upstream of the two locations obtained through FFT is very weak. However, considering the non-stationary characteristics of fluctuant wind, the time-frequency coherence of wind between upstream of these two locations is then analyzed using wavelet transform and the wind of upstream between these two locations has stronger correlation in low frequency. Thus, the temporal information of wind should be used in estimation of buffeting response of a bridge.
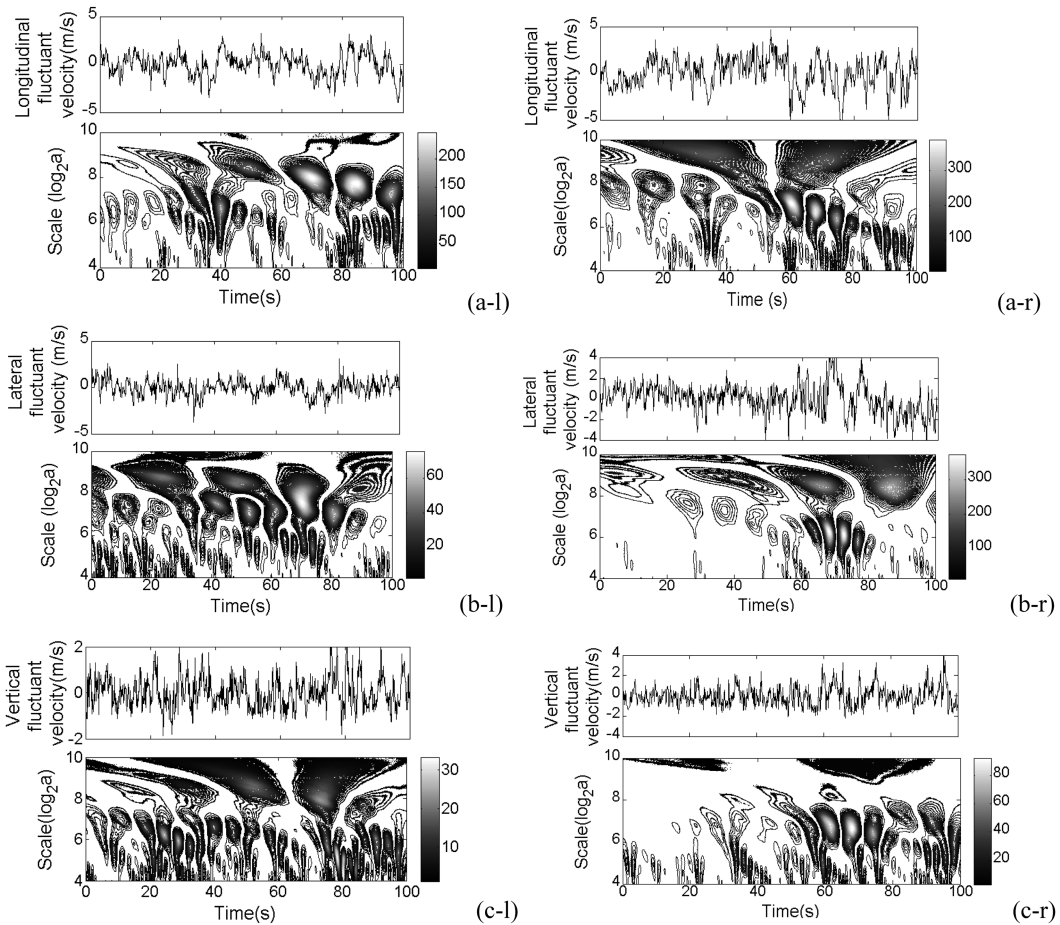
Fig. 35 Contour plots of square wavelet coefficients of fluctuant wind in wake-flow of M3 (left) and M6
(right) (a) longitudinal, (b) lateral and (c) vertical

(4) The non-stationary characteristics of fluctuant wind are analyzed using wavelet transform. It is observed that nature fluctuating wind is highly intermittent and has distinct coherence structures. However, the intermittent structures appear at different time at upstream of M3 and M6. The analysis on fine structures in time-frequency domain indicates that the energy distributions of the wind in time have self-similarity.

(5) The full-scale flow characteristics around the bridge deck is investigated and found that the mean wind speeds decrease after the inflow passing through the bridge deck, the turbulence intensities in wake-flow become very large and the turbulence integral lengths become very small.

Acknowledgements

References

Azarbayejani, M., EI-Osery, A.I. and Reda Taha, M.M. (2009), "Entropy-based optimal sensor networks for structural health monitoring of a cabled-stayed bridge", *Smart Struct. Syst.*, **5**(4), 369-379.

Bietry, J., Delaunay, D. and Conti, E. (1995), "Comparison of full-scale measurement and computation of wind effects on a cable-stayed bridge", *J. Wind Eng. Ind. Aerod.*, **57**, 225-235.

Boldes, U., Scarabino, A., Marañon Di Leo, J., Colman, J. and Gravenhorst, G. (2003), "Characteristics of some organized structures in the turbulent wind above and within spruce forest from field measurements", *J. Wind Eng. Ind. Aerod.*, **91**, 1253-1269.

Chabalko, C.C., Jordan, D.A., Hajj, M.R. and Tieleman, H.W. (2005), "Characteristic time scales of velocity and pressure events", *J. Fluid. Struct.*, **20**(8), 1057-1071.

Dunyak, J., Gilliam, X.N., Peterson, R. and Smith, D. (1998), "Coherent gust detection by wavelet transform", *J. Wind Eng. Ind. Aerod.*, **77-78**, 467-478.

Frandsen, J.B. (2001), "Simultaneous pressures and accelerations measured full-scale on the Great Belt East suspension bridge", *J. Wind Eng. Ind. Aerod.*, **89**(1), 95-129.

Fu, J.Y., Li, Q.S., Wu, J.R., Xiao, Y.Q. and Song, L.L. (2008), "Field measurements of boundary layer wind characteristics and wind-induced responses of super-tall buildings", *J. Wind Eng. Ind. Aerod.*, **96**(8-9), 1332-1358.

Gurley, K., Kijewski, T. and Kareem, A. (2003), "First- and higher-order correlation detection using wavelet transforms", *J. Eng. Mech.-ASCE*, **129**(2), 188-201.

Hajj, M.R., Jordan, D.A. and Tieleman, H.W. (1998), "Analysis of atmospheric wind and pressures on a low-rise building", *J. Fluid. Struct.*, **12**, 537-547.

Jang, S., Jo, H., Cho, S., Mechitov, K., Rice, J.A., Sim, S.H., Jung, H.J., Yun, C.B., Spencer Jr, B.F. and Agha, G. (2010), "Monitoring of a cable-stayed bridge using smart sensor technology: deployment and evaluation", *Smart Struct. Syst.*, **6**(5-6), 439-459.

Kareem, A. and Kijewski, T. (2002), "Time-frequency analysis of wind effects on structures", *J. Wind Eng. Ind. Aerod.*, **90**, 1435-1452.

Ko, J.M. and Ni, Y.Q. (2005), "Technology developments in structural health monitoring of large-scale bridges", *Eng. Struct.*, **27**(12), 1715-1725.

Li, H., Ou, J.P., Zhao, X.F., Zhou, W.S., Li, H.W., Zhou, Z. and Yang, Y.S. (2006), "Structural health monitoring system of the Shandong Binzhou Yellow River Highway Bridge", *Comput.-Aided Civ. Inf.*, **21**(4), 306-317.

Miyata, T., Yamada, H., Katsuchi, H. and Kitagawa, M. (2002), "Full-scale measurement of Akashi-Kaikyo Bridge during typhoon", *J. Wind Eng. Ind. Aerod.*, **90**, 1517-1527.

Ni, Y.Q., Ko, J.M., Hua, X.G. and Zhou, H.F. (2007), "Variability of measured modal frequencies of a cablestayed bridge under different wind conditions", *Smart Struct. Syst.*, **3**(3), 341-356.

Ou, J.P. and Li, H. (2010), "Structural health monitoring in mainland China: review and future trends", *Struct. Health Monit.*, **9**(3), 219-231.

Terradellas, E., Morales, G., Cuxart, J. and Yague, C. (2001), "Wavelet methods: application to the study of the stable atmospheric boundary layer under non-stationary conditions", *Dynam. Atmos. Oceans*, **34**(2-4), 225-244.

Xu, Y.L. and Zhu, L.D. (2005), "Buffeting response of long-span cable-supported bridges under skew winds, Part 2: case study", *J. Sound Vib.*, **281**(3-5), 675-697.

CC